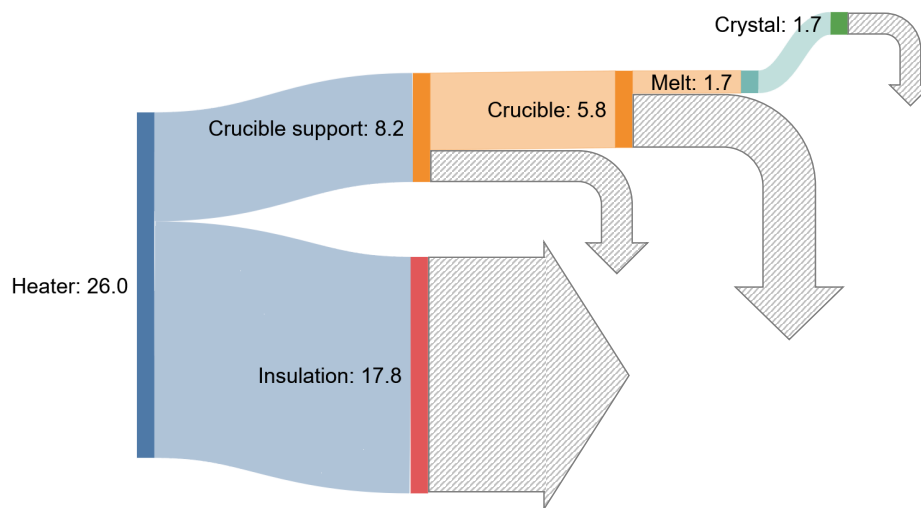


Graphical Abstract

Heating efficiency and energy saving potential of Czochralski crystal growth furnaces

Sepehr Foroushani, Arved Wintzer, Frank-Michael Kiessling, Kaspars Dadzis



Highlights

Heating efficiency and energy saving potential of Czochralski crystal growth furnaces

Sepehr Foroushani, Arved Wintzer, Frank-Michael Kiessling, Kaspars Dadzis

- Methodology to analyze energy efficiency of crystal growth processes is proposed.
- Heat flows from power sources to cooling water are measured in a growth furnace.
- Induction heating demonstrates 35% higher efficiency compared to resistance heating.
- Numerical thermal model is validated within 20% of the measurements.
- Simulations suggest only 20% of heating power in a silicon growth furnace is delivered to the crucible.

Heating efficiency and energy saving potential of Czochralski crystal growth furnaces

Sepehr Foroushani^a, Arved Wintzer^a, Frank-Michael Kiessling^a, Kaspars Dadzis^{a,*}

^a*Leibniz-Institut für Kristallzüchtung (IKZ), Max-Born-Str. 2, Berlin, 12489, Germany*

Abstract

Environmental concerns and rising energy costs have increased attention to energy efficiency in growing semiconductor crystals from melt, traditionally a highly energy-intensive process. The energy conservation measures have so far generally been limited to the ventilation and air-conditioning of production facilities, with far less attention paid to the process equipment. In the present work, a thermodynamic limit is established as the baseline for evaluating the energy efficiency of industrial crystal growth processes. It is then shown that the typical industrial furnace has energy demands far above this strictly necessary limit. Measurements on a research-scale furnace with induction and resistance heating along with numerical simulation with validated models are used to identify the sources of energy loss in the furnace and possible ways of improving energy efficiency. Measurement results show that switching to induction heating can lead to energy savings of roughly 35%. Simulations demonstrate the utility of numerical modes in gaining a detailed understanding of the thermal performance of the furnace and identifying the improvement and optimization measures.

Keywords: A1. Heat transfer, A1. Power consumption, A1. In-situ measurements, A1. Computer simulation, A2. Czochralski method, B2. Semiconducting silicon

1. Introduction

Semiconductors are an indispensable part of the modern world. For most applications, e.g. power electronics, solar energy, quantum computing and photonics, semiconductors are needed in crystalline form. Semiconductor crystals are mostly grown from melt, using various techniques such as Czochralski (CZ), floating zone (FZ) and Vertical Gradient Freeze (VGF). All these methods entail the initial melting of raw materials, e.g. polycrystalline silicon, and subsequent solidification of the melt in a controlled manner in order to achieve a single crystal with the desired characteristics. The CZ technique entails the melting of the raw material in a crucible using resistance (e.g. for silicon [1]) or induction (e.g. for Ga_2O_3 and other high-melting oxides [2]) heating, followed by the dipping a single-crystal seed into the melt. Under simultaneous rotation and upward pulling, the melt solidifies around the seed and a crystal grows. See the references above for further details.

*

Email address: kaspars.dadzis@ikz-berlin.de (Kaspars Dadzis)

Two factors make the growth of semiconductor crystals energy intensive: i) the high melting points, e.g. Si at 1410 °C and Ga₂O₃ at 1900 °C, and ii) the high heats of fusion, e.g. 1800 kJ/kg for silicon.¹ Other than the energy intensity of crystal growth, the high energy demand of semiconductor production can be attributed to the strict clean-room requirements such as the circulation of filtered air at high rates and tightly controlled room temperature and humidity [4, 5]. It is estimated that heating, ventilation and air conditioning (HVAC) systems represent around 30% of the electricity demand of a typical semiconductor fabrication facility [6], while figures as high as 54% have also been reported [7].

While sustainability and environmental concerns have, over the past few decades, gradually raised the profile of energy efficiency in various industries including semiconductor production, the recent surge in energy prices in Europe [8] have shot energy efficiency onto the top of priority lists across virtually all sectors. The energy intensity of silicon wafer production is generally acknowledged [9] and has been studied to some extent, particularly for photovoltaics [10, 6]. Nevertheless, the energy conservation measures have generally been limited to HVAC systems, with far less attention paid to the process equipment [7], particularly the crystal growth furnaces. See [11, 12], for instance, for studies of the energy demand of solar-grade silicon production.

Figure 1 shows representative values for the energy intensity of silicon production and three main sub-processes: i) smelting, i.e. is the heating of silica (quartz) beyond its melting point in the presence of reducing agents, ii) the Siemens process, widely used for upgrading metallurgical silicon to solar-grade, and iii) crystal growth (CZ and FZ processes). In the absence of process-specific data from the crystal growth industry, crude estimates were obtained based on typical heating power, growth rate and crystal diameter. See Appendix A for details. These estimates are in line with estimates used in the literature, e.g. 6 – 30 kWh/kg in [10] or 13 kWh/kg in [9]. In Figure 1, the energy intensity of steel and aluminum production, widely used as examples of energy-intensive processes, are also shown as reference. It can be seen that, in its energy intensity, silicon crystal growth is comparable to the production of steel and aluminum.²

In Figure 1, a thermodynamic limit for the energy intensity of silicon crystal growth (1.1 kWh/kg) is shown as reference. See Appendix A for the details of how this limit was estimated. According to Figure 1, silicon crystal growth consumes up to 20 times the strictly required energy (thermodynamic limit). This large gap indicates a significant potential for improving the thermal design of crystal growth furnaces and processes and motivates the present study.

The present work aims to identify the sources of the significant gap between the ideal and actual crystal growth processes with respect to energy consumption and possible ways of reducing that gap. The flow of energy from power supply to the melting crucible is examined using a combination of experiment and numerical simulation. The study is limited in scope to the prominent Czochralski (CZ) process. Both induction and resistance heating are considered.

¹As reference, consider the melting point and heat of fusion of common metals iron (1536 °C, 272 kJ/kg) and aluminum (660 °C and 388 kJ/kg) [3].

²Note that the yearly production quantities [13] of silicon metal (3,800,000 tons), aluminum (70,000,000 tons) and steels (1,900,000,000 tons) are vastly different.

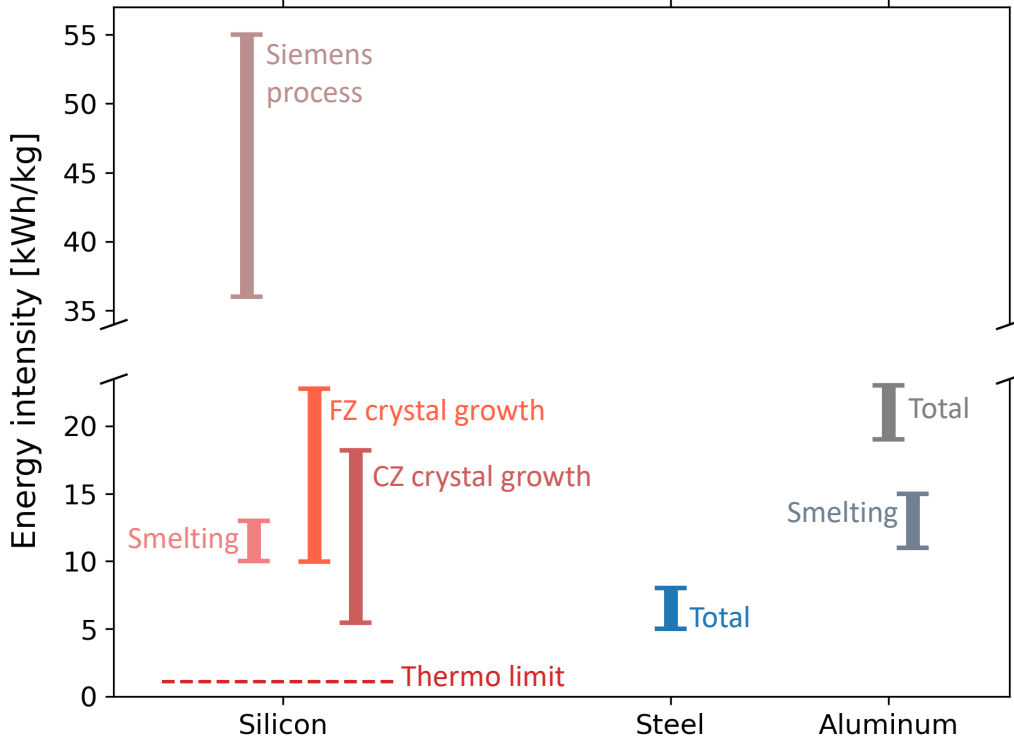


Figure 1: Energy intensity of the production of silicon, steel and aluminum.

Sources: Siemens process [12], silicon smelting [11], steel [14], aluminum [15, 16], aluminum smelting [16]. Thermo limit and CZ/FZ crystal growth estimated as shown in Appendix A.

The remainder of this paper is organized as follows. In the next section, the experimental setup and measurement methods are described and select measurement results are presented. Section 3 presents a brief description of the numerical model used for the present study and its validation against the experimental data. In Section 4, the validated model is applied to an industrial-scale process and the flow of energy to and from the furnace’s hot zone is traced. A summary of the main findings and perspectives for future work conclude the paper.

2. Experiments

2.1. Setup

Experiments were conducted in a research-scale crystal growth facility consisting of a stainless steel furnace with nearly cylindrical interior (inner diameter: 263 mm, height: 383 mm). See Figure 2. The furnace is supported by a profile structure and equipped with top and bottom shafts that can be rotated and translated axially. A large front door and flanges at various heights on both sides as well as on the door allow the installation and operation of various sensors and heating setups. The furnace can be operated under different atmospheres – air, nitrogen or argon – and pressures ranging from atmospheric down to about 10^{-3} mbar. The furnace walls, shafts and parts of the power supply circuit are water-cooled. The design of furnace and feedthroughs preclude temperatures above 1000 °C in the furnace. Further details on the experimental setup can be found in [17]. For the present measurements, two glass viewports were installed on the front door ISO-K

DN63 flanges, while the side flanges which were not used for instrumentation or electrical connections were blinded.

Measurements were made with two separate heating systems: i) an induction heater consisting of a hollow, water-cooled induction coil (inner diameter: 140 mm) made of a copper pipe (outer diameter: 10 mm, wall thickness: 2 mm) with three windings, and ii) a meander-shaped cylindrical resistance heater made of graphite (inner diameter: 110 mm, thickness: 4.5 mm, resistance: approximately 125 m Ω at room temperature). The induction coil was powered by a generator with a maximum power of 30 kW (Trumpf TruHeat MF 5030). In the present study, the induction coil operated at around 14 kHz. The resistance heater was powered by a transformer with a maximum power of 4.2 kW and maximum secondary voltage of 22 V at 50 Hz (BREMER GmbH). The power supply circuitry and cooling water loops of both heating systems are schematically shown in Figure 3.

The power supply was regulated using a controller (Eurotherm Advanced Temperature Controller 3504) based on target temperature or power supply setpoints (generator output voltage for induction heater and thyristor output power for resistance heater). The crucible temperature was monitored using a Type K thermocouple inserted about 20 mm deep into the crucible wall from the top. Additionally, two short-wavelength (2 – 2.6 μ m) pyrometers [Advanced Energy (LumaSense) IGA 6/23 Advanced, IGAR 6 Advanced], sighted through a glass viewport, were used to monitor the temperature of the crucible and resistance heater, with the emissivity of graphite assumed constant at 0.8 based on earlier in-house measurements [18].

2.2. Measurement of heating power and cooling rate

In order to assess the energy performance of the furnace, heating tests were performed where cylindrical crucibles made of graphite were heated under nitrogen and vacuum atmospheres. Assuming that the melt and crystal have a small influence on the thermal performance of the furnace, they were excluded from the heating tests. The heating power and cooling rates were measured as described in the following sections. Due to the continuous development of the experimental setup, the crucibles and insulation used in the two heating setups were different. The crucible used in induction heating had outer diameter and height of respectively $D_{\text{cruc}} = 120$ mm and $H_{\text{cruc}} = 45$ mm while the resistance heating crucible had $D_{\text{cruc}} = 70$ mm and $H_{\text{cruc}} = 65$ mm. See Figure 2.

Heating power. Differential voltage probes (Keysight N2791a, Testec TT-SI 9101) and Rogowski current sensors (Chauvin Arnoux MA200) along with an oscilloscope (Keysight InfiniiVision DSOX1204G) were used to measure the supply voltage and current. The measurement points are shown Figure 3. The voltage and current signals were of truncated sinusoidal (phase-cut by thyristor) form in resistance heating and full sinusoidal form in induction heating. Measurements were made over at least three periods with sampling rates of at least 1.5×10^5 Hz for resistance heating and at least 4×10^7 Hz for induction heating. With the voltage (U) and current (I) signals obtained from oscilloscope measurements, the heating power was calculated based on the formula:

$$P = \frac{1}{\tau} \int_t^{t+\tau} U(t) I(t) dt \quad (1)$$

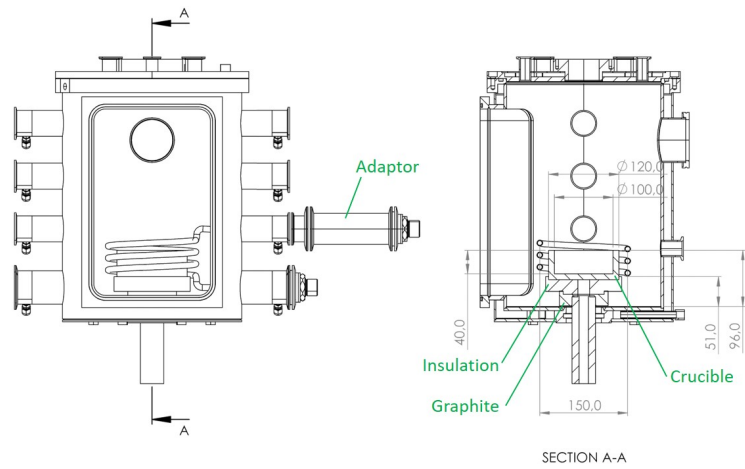
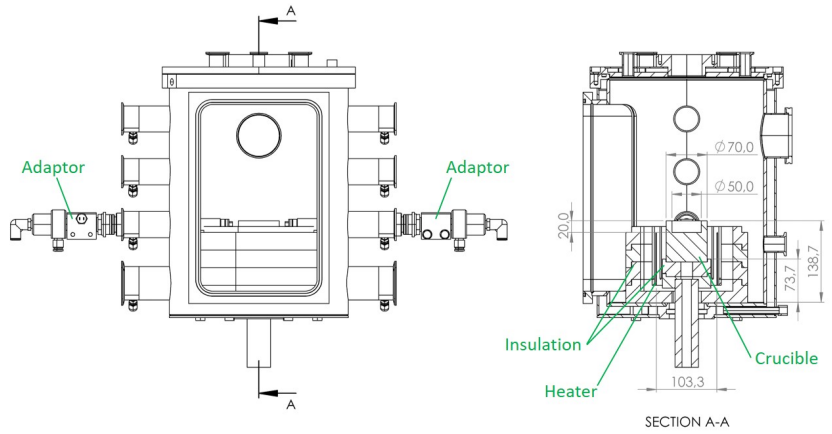
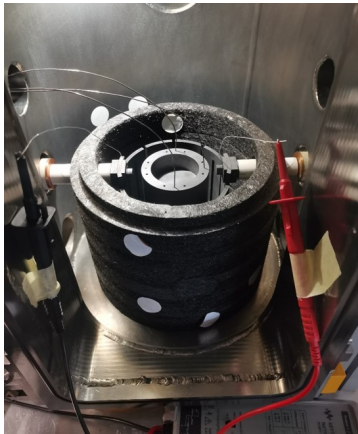


Figure 2: Research crystal growth furnace with resistance (TOP) and induction (BOTTOM) heating setups

where t denotes time and τ denotes the signal period. Note that, in the case of induction heating, Equation 1 gives the effective (real) power. The integral was evaluated numerically.

Cooling rate. The volumetric flow rate, \dot{V} , and inlet and outlet temperatures, T_{in} and T_{out} , of cooling water in various loops were measured using magnetic-inductive flow meters (ifm SM8020 for the common inlet) and vortex flow meters (ifm electronic SV4200 for all returns) with integrated temperature sensors. The measurement points are shown in Figure 3. The inlet temperature and the flow rates in various loops were nearly constant throughout each experiment. Therefore, thermal steady state was determined based on the outlet cooling water temperatures. The cooling rate in loop i was then estimated based on a steady-state energy balance of the cooling water, as shown in Equation 2, with the density and specific heat of water assumed constant at $\rho = 1000 \text{ kg/m}^3$ and $C_p = 4180 \text{ J/(kg K)}$, respectively.

$$Q_i = \rho \dot{V}_i C_p (T_{\text{out},i} - T_{\text{in}}) \quad (2)$$

Uncertainty. The nominal accuracy of the devices used for measuring the heating power and cooling rate are listed in Table 1. Even from these nominal values, it can be seen that the cooling rate measurements have a much higher uncertainty than the electrical power measurements.

Table 1: Nominal accuracy of measurement devices for heating power and cooling rate

Parameter	Measurement device	Nominal accuracy
Current	Rogowski coil (Chauvin Arnoux MA200)	1% + 0.3 A [19]
Voltage	Differential probe (Keysight N2791a, Testec TT-SI 9101)	2% [20, 21]
Return flow rate	Vortex flow meter (ifm SV4200)	0.04 lit/min [22]
Return flow temperature	Vortex flow meter (ifm SV4200)	1 K [22]
Supply flow temperature	Magnetic-inductive flow meter (ifm SM8020)	2.5 K [23]

Results: energy balance of the furnace. In Figure 4, the measured steady-state power and cooling rates for resistance heating are shown under nitrogen (1 bar) and vacuum ($\sim 3 \times 10^{-5}$ bar) atmospheres. In each case, the measured RMS current is also shown for reference (plotted against the axis on the right). Comparing the power supplied to the furnace, P_{furn} , and the total rate of cooling by water, Q_{tot} , it can be seen that the discrepancy between P_{furn} and Q_{tot} increases with temperature. While for $T_{\text{cruc}} \lesssim 500 \text{ }^\circ\text{C}$, $P_{\text{furn}} \approx Q_{\text{tot}}$ (within measurement error), the difference increases with T_{cruc} , reaching $\sim 500 \text{ W}$ at $T_{\text{cruc}} = 800 \text{ }^\circ\text{C}$. This discrepancy can be explained by thermal radiation through the glass viewports, noting that, in resistance heating, the graphite heater constitutes a heat source which, according to measurements, can be up to $\sim 150 \text{ }^\circ\text{C}$ hotter than the crucible. The same general trend is observed by comparing power loss in the flange adaptors (see Fig. 3), P_{loss} , estimated as the difference between the power measured at the furnace (outside) and at the heater (inside), and Q_{conn} , the rate of cooling of the

adaptors. From Figure 4 it can further be seen that the highest cooling rate occurs in the furnace walls, which, given the large interior surface area of the furnace, is to be expected. While the qualitative observations above are also valid for heating under vacuum (Figure 4-bottom), it can be seen that, compared to nitrogen atmosphere, the required heating power to achieve a certain temperature is much lower under vacuum — up to 36% lower for $T_{\text{cruc}} \approx 800$ °C.

In Figure 5, the measured steady-state power and cooling rates are shown for induction heating under nitrogen (1 bar). Examining the overall energy balance of the furnace, it can be seen $P_{\text{furn}} \approx Q_{\text{tot}}$, even at higher temperatures, which confirms the hypothesis that the relatively large difference between P_{furn} and Q_{tot} in resistance heating is due to radiation from the graphite heater which finds its way out of the furnace through the glass viewports.³

The higher efficiency of induction heating in comparison to resistance heating can be seen by comparing Figure 5-top and Figure 4-top. Achieving $T_{\text{cruc}} \approx 800$ °C with induction heating requires 34% less power compared to resistance heating (4.13 kW vs 2.79 kW), although the induction heating crucible has a larger diameter and was not insulated in the heating tests reported here. In fact, the results of induction heating under atmospheric nitrogen are comparable to those of resistance heating under vacuum. To better illustrate the energy balance of the furnace with the two heating systems, the results for $T_{\text{cruc}} \approx 800$ °C with the two heating methods under nitrogen are plotted in Figure 6.

Noting that, under vacuum, radiation is the dominant mode of heat transfer, the measurement results could be approximately scaled to other temperatures (T) as well as crucible diameters (D) and heights (H), as:

$$P_2 \approx P_1 \left(\frac{H_2}{H_1} \right) \left(\frac{D_2}{D_1} \right) \left(\frac{T_2}{T_1} \right)^4 \quad (3)$$

Note that such a scaling does not take account of differences between the hot-zones of the highly simplified measurement setup presented here and, e.g., a furnace for CZ growth of 300 mm silicon crystals. Nevertheless, it can be reasonably assumed that the projected difference in the energy intensity of induction and resistance heating are also indicative for an industrial silicon growth furnace.

2.3. Measurement of magnetic field

Accurate modeling of the magnetic field induced by the coil is essential for accurate simulation of induction heating in the furnace. In order to enable robust validation of the electromagnetic model (described in Section 3), measurements of the magnetic field inside the furnace were performed.

Measuring the magnetic flux density in the kHz frequency range is challenging as there are limited devices and sensors that are readily applicable. In the present study, a Hall-effect sensor (Honeywell SS495A) was used to measure the density of the magnetic field induced by the coil. The sensor was supplied with 5 V_{DC} using a source-meter (Keithly 2450

³The hypothesis was further confirmed by examining the relation between the discrepancy and temperature; it was found that $P_{\text{furn}} - Q_{\text{tot}} \sim T_{\text{cruc}}^4$ where $[T_{\text{cruc}}] = \text{K}$.

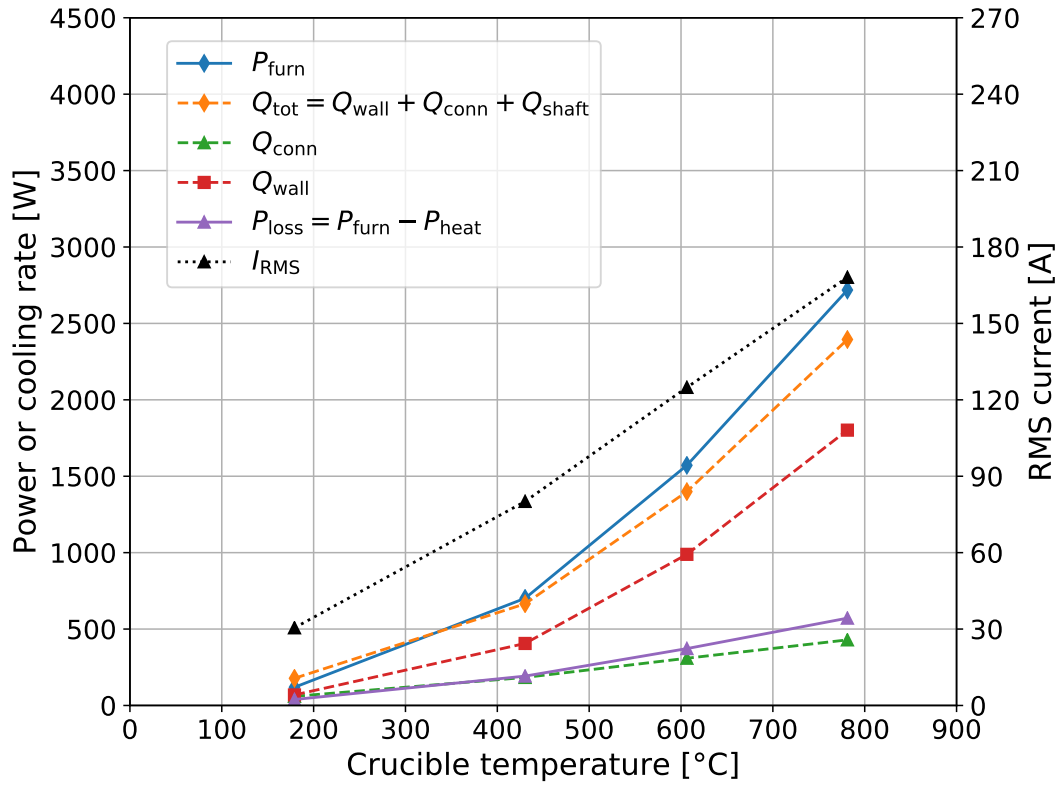
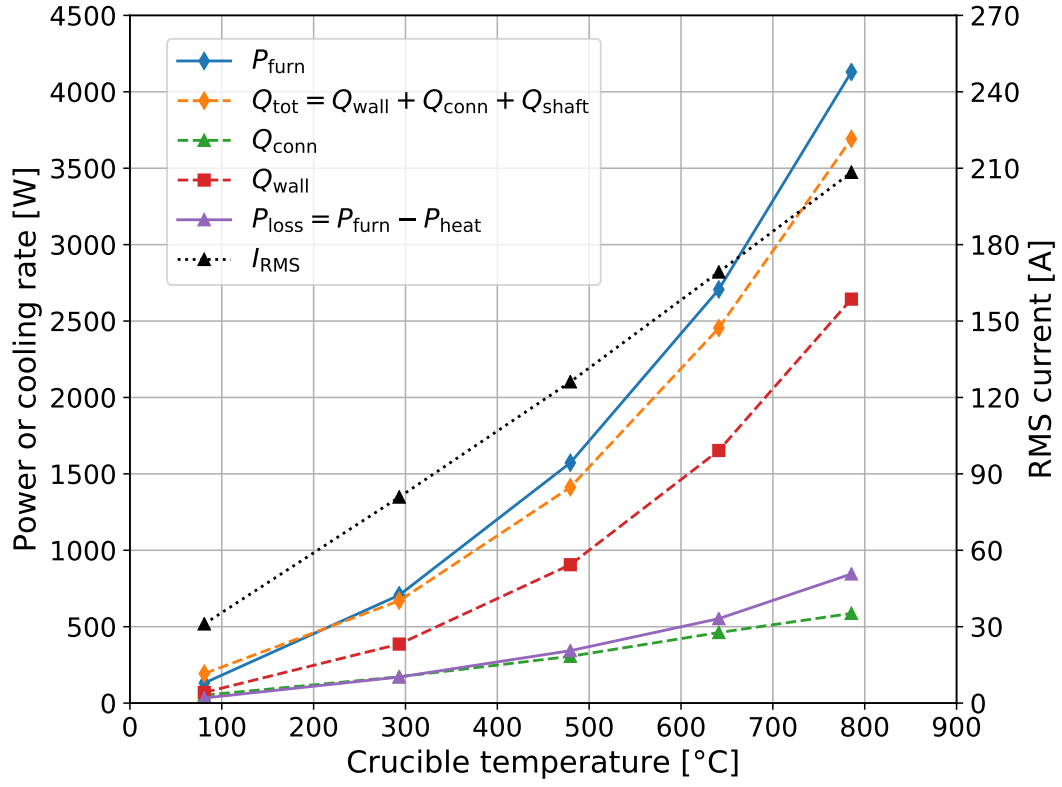


Figure 4: Steady-state current, power and cooling rates with **resistance** heating under N₂ (TOP) and vacuum (BOTTOM).

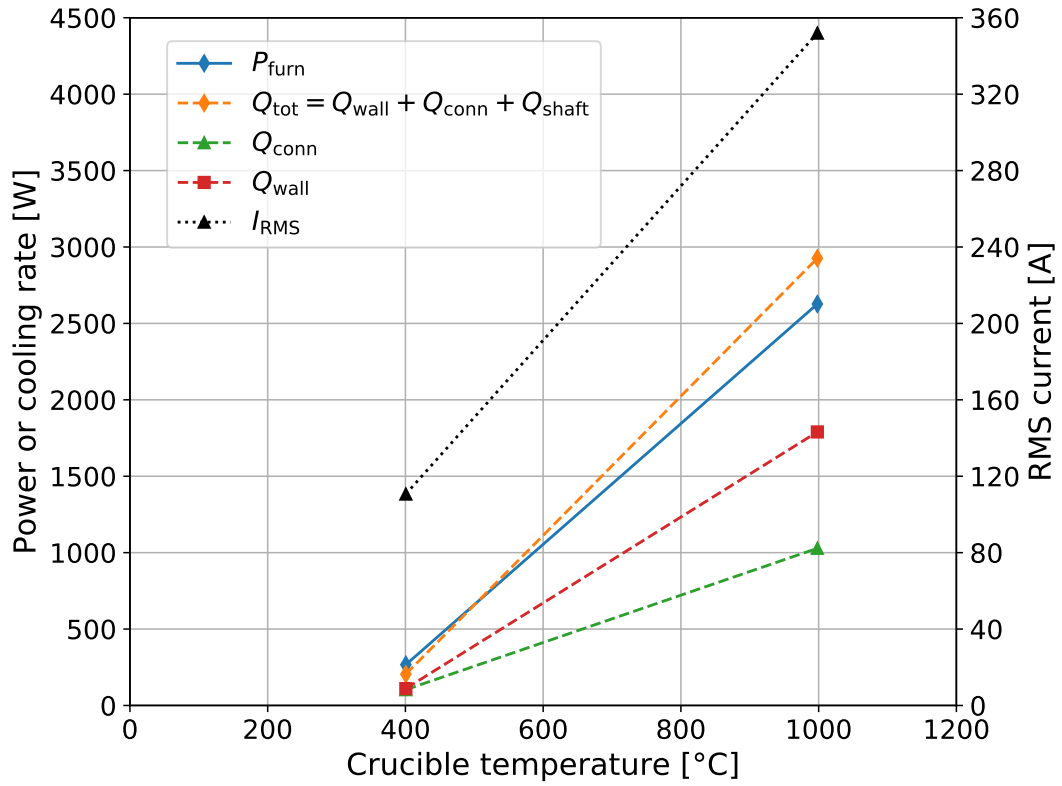
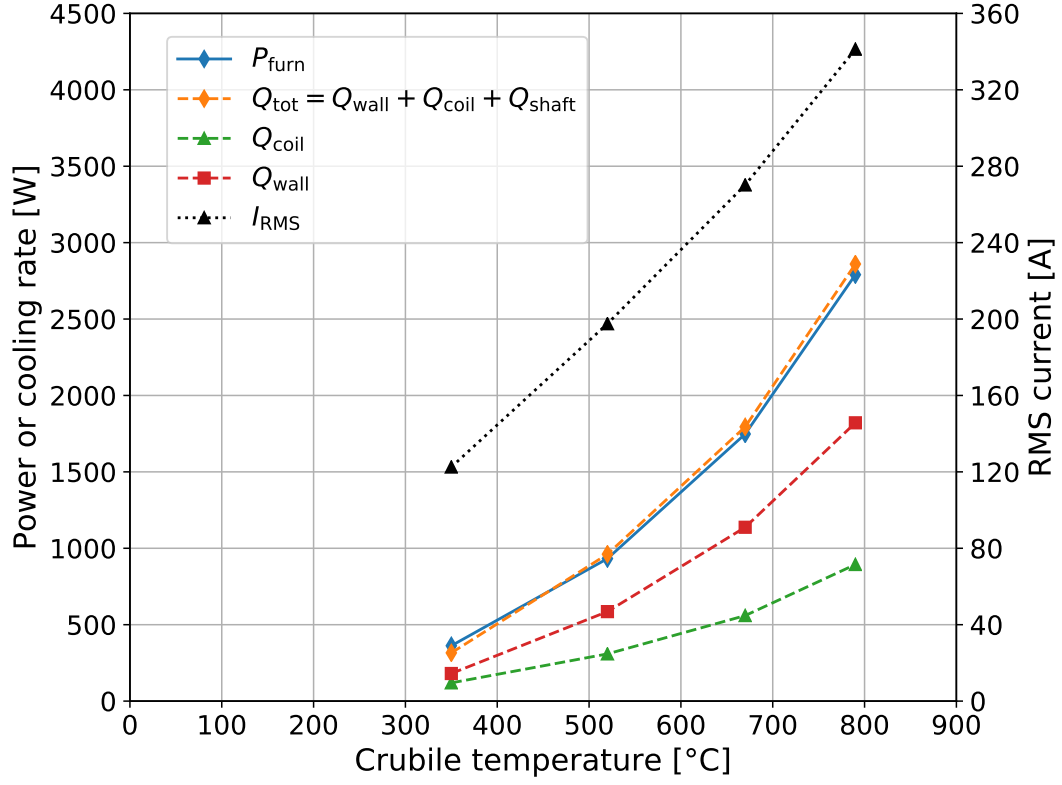


Figure 5: Steady-state current, power and cooling rates with **induction** heating under N₂ (TOP) and vacuum (BOTTOM). Note the difference in the horizontal axis scales.

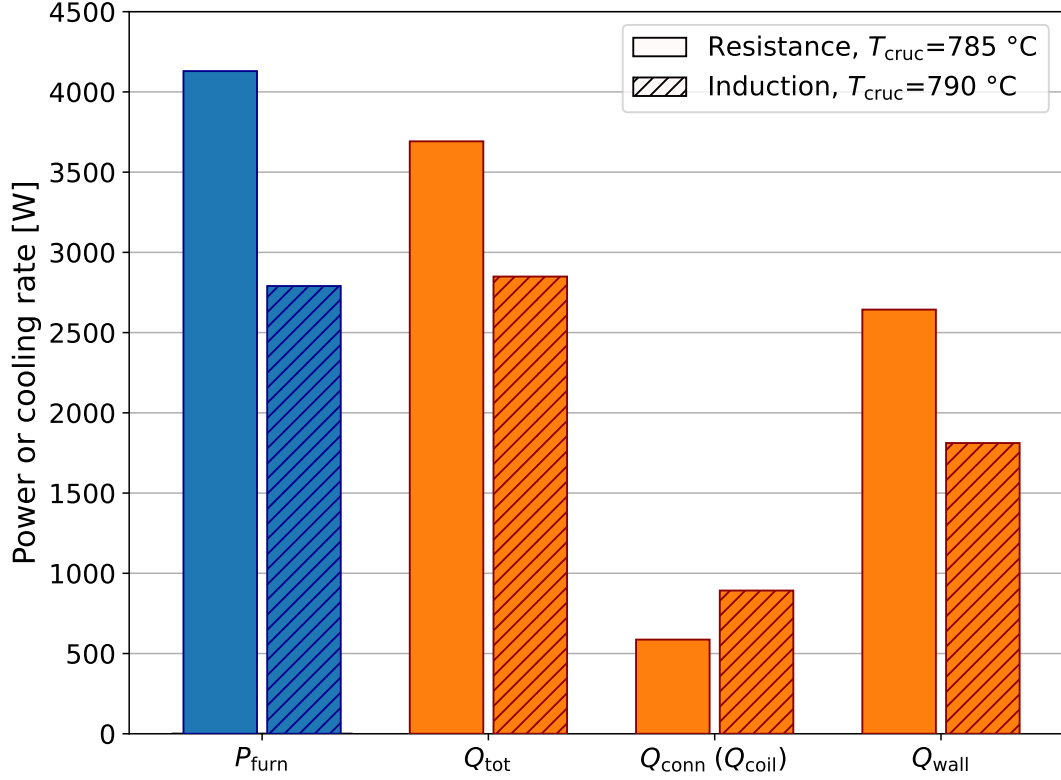


Figure 6: Steady-state power and cooling rates under N_2 : resistance ($D_{\text{cruc}} = 70\text{ mm}$) vs. induction heating ($D_{\text{cruc}} = 120\text{ mm}$).

SourceMeter). A multi-meter (Keithly DAQ6510) was used to record the output voltage.⁴ An in-house calibration was undertaken to verify the manufacturer’s calibration for the present study’s frequency range, as outlined in [Appendix B](#). The sensor was attached to a ceramic holder, as shown in [Figure 7](#). Note that the sensor responds to magnetic flux normal to its surface (i.e. along the ceramic holder; see [Figure 7](#)). Azimuthal and axial profiles of the magnetic flux density in the axial direction (B_z) were obtained by slowly moving the sensor in the circumferential ($\sim 0.1\text{ rpm}$) and axial ($\sim 10\text{ mm/min}$) directions, starting at various radial and axial positions, and recording the signal at approximately two-second intervals. Measurement results are discussed in [Section 3.2](#).

⁴Since the magnetic field of an induction coil is alternating, the output Hall voltage is alternating too. Here, the multi-meter was set to record the RMS voltage.



Figure 7: LEFT: Hall sensor attached to a ceramic holder, RIGHT: Hall sensor and holder during measurement in the furnace.

3. Simulations

3.1. Model description

The multiphysics finite-element solver Elmer [24] was used for modeling electromagnetism, heat transfer and phase change, as described in previous work [25]. In the present study, steady-state solutions to time-harmonic electromagnetics, heat transfer, and phase change models were performed in the following order:

- First, electromagnetism was solved, and Joule heating in the electrically conducting components was computed.
- Next, heat transfer was solved with Joule heating from the electromagnetism solution as source term.
- Finally, phase change was evaluated and the crystallization front was shifted into the isothermal of the melting point.

For the growth process, this procedure was repeated iteratively. For heating tests, which were simulated using constant material properties without phase change, no iteration was required.

For the simulation of time-harmonic 2D axisymmetric electromagnetic fields, an equation for the complex vector potential A (azimuthal component)

$$\nabla \times \left(\frac{1}{\mu_0} \nabla \times A_\phi \mathbf{e}_\phi \right) + i\omega\sigma A_\phi \mathbf{e}_\phi = j_{s\phi} \mathbf{e}_\phi \quad (4)$$

was solved with μ_0 denoting the magnetic permeability of free space, ω denoting angular frequency, and σ denoting electric conductivity, assuming an equal distribution of the source current $j_{s\phi}$ over the volume of the inductor. It should be noted that a constant input current was applied as boundary condition for electromagnetic simulations, which did not necessarily match the real (measured) value. The actual current was instead computed in post-processing based on a scaling of the heater power as described below.

Steady-state heat transfer calculation was based on

$$-\nabla \cdot (\kappa \nabla T) = h , \quad (5)$$

with κ denoting thermal conductivity, T denoting temperature, and h the volumetric source term. For induction heating, the heat source term from the electromagnetism simulation was applied, which is given by

$$h = \frac{|j|^2}{2\sigma} = \frac{\Re(j)^2 + \Im(j)^2}{2\sigma} = \sigma\omega^2 \frac{\Re(A_\phi)^2 + \Im(A_\phi)^2}{2} , \quad (6)$$

where \Re denotes the real part and \Im denotes the imaginary part. For resistance heating, an equally distributed heater power over the volume of the heater was assumed. This heat source term was scaled so that the desired temperature (as measured) was reached. The obtained factor was then applied in post-processing to scale the results, i.e., current density, Lorentz force, or magnetic flux density. Heat radiation between the boundaries of all solid parts of the furnace was modeled under the assumption of diffusive grey surfaces and using Gebhart factors [26].

Phase change in 2D was solved in a steady-state approximation, where the position of the crystallization front is determined based on the isotherm at the melting point and the latent heat release according to

$$q_\ell - q_s = L\rho_s v_s , \quad (7)$$

with q_s and q_ℓ denoting heat fluxes in the normal direction to the crystallization front on the solid and liquid sides respectively, L the latent heat, ρ_s the solid density, and v_s the solidification speed. The mesh boundary between crystal and melt is then moved to the new position.

The finite element mesh generator Gmsh [27] was used to create unstructured grids of triangular 2nd-order elements for the simulations. A further discussion of model verification and grid dependence can be found in [28].

3.2. Validation

Heat transfer. The thermal model was validated by comparing the simulation results for heating power (P) and selected cooling rates (Q) with the measurements. The computational domains for heating tests with resistance and induction heaters include an empty crucible and the induction coil or the resistance heater with insulation as shown in Figure 2 and described in Section 2.2. Calculation files including the source code of the model in Elmer can be found in [29].

In Figure 8 the simulation and measurement results for resistance heating are shown. It can be seen that, for the same crucible temperature of 780 °C, the simulation result for the heater power P_{heater} is 24% smaller than measured in the experiment. Consequently, the heat transfer rate Q_{wall} in the furnace walls is also smaller than the measured cooling rate. The higher heating power in the experiments can be explained by the heat loss in heater connections, Q_{conn} , which were not included in the numerical model. Note that this heat loss may also cause the higher cooling rate in the furnace wall.

The case with induction heating, shown in Figure 9, demonstrates an opposite trend, where, for the crucible temperature of 1000 °C, the simulation result for the inductor power P_{furnace} is 15% higher than measurements. The heat transfer rate to the furnace

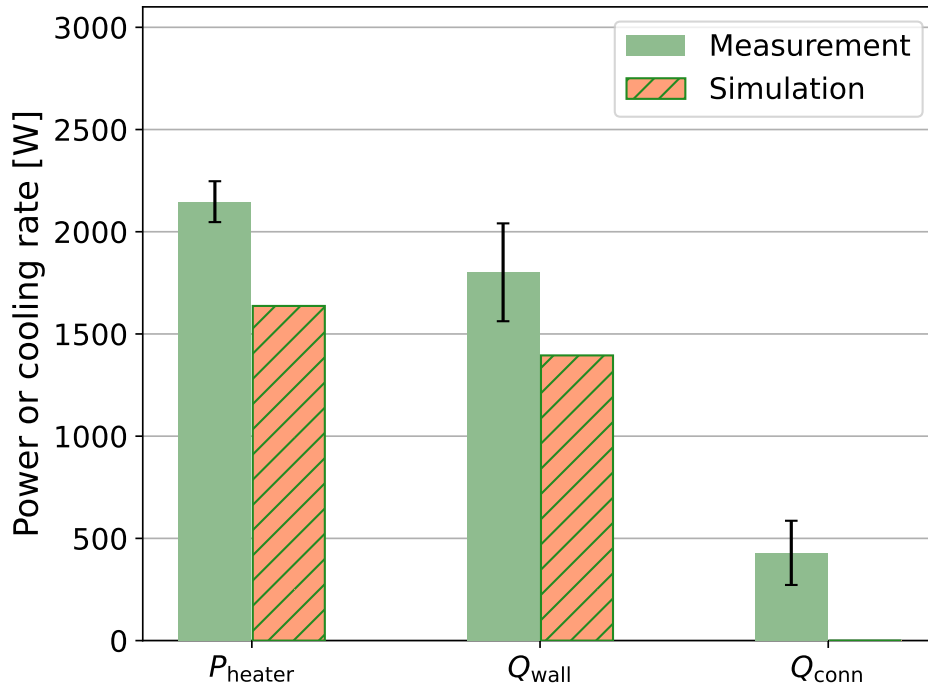


Figure 8: Comparison of simulation and measurement results for heating power and cooling rates with resistance heating under vacuum at $T_{\text{cr}} = 780$ °C.

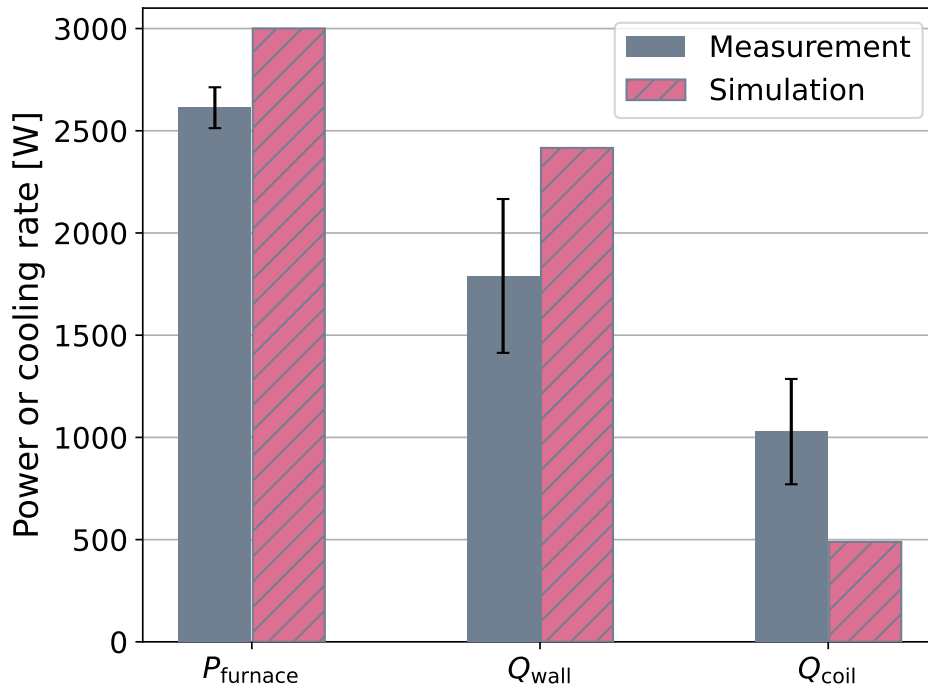


Figure 9: Comparison of simulation and measurement results for heating power and cooling rates with induction heating under vacuum at $T_{\text{cr}} = 1000$ °C.

walls Q_{wall} is also higher in simulations, while the heat losses in the water-cooled coil Q_{coil} are lower. The latter can be explained by local heating of the feedthroughs in the experiment. At this stage of model development, it is assumed that the discrepancy in heating power is likely caused by inaccurate electrical conductivity of graphite or the simplified 2D modeling of the induction coil.

In both Figures 8 and 9, the error bars show the larger of the standard deviation of values from repeated measurements during the experiment and the nominal error from simple propagation of the accuracies shown in Table 1.

It can be concluded that the simulations are able to reproduce the heating powers and cooling fluxes with acceptable accuracy even with relatively simple 2D models. It must be emphasized that the comparison presented pertains to vacuum conditions and the modeling accuracy could be significantly reduced by convective heat transfer, in particular at low temperatures where heat radiation is not dominant [25].

Electromagnetics. In order to validate the electromagnetic model, simulations of the magnetic field induced by the coil, in the absence of the crucible, were compared to measurements in the model furnace (Section 2.3). In Figure 10, simulated and measured magnetic flux densities are shown along two vertical lines: i) inside the coil, close to the copper windings ($r = 60 \text{ mm}$, $\phi = 270^\circ$), and ii) along the coil center ($r = 0$). Along $r = 60 \text{ mm}$, $\phi = 270^\circ$, the simulation shows a higher peak than the measurement, with a maximum deviation of 6% within the coil ($50 \lesssim z \lesssim 110 \text{ mm}$). Along $r = 0$, the simulated peak (at $z = 86 \text{ mm}$) is 12% lower than the measurement, with the relative difference between the simulation and measurement results almost constant, i.e. independent of z . The observed deviations in both profiles can be attributed to simplifications in modeling the coil geometry and the assumption of evenly distributed current density. The overall agreement between simulations and measurements and the ability of the model in reproducing the magnetic flux density profiles were taken as indications of the validity of the model. Further details can be found in [28].

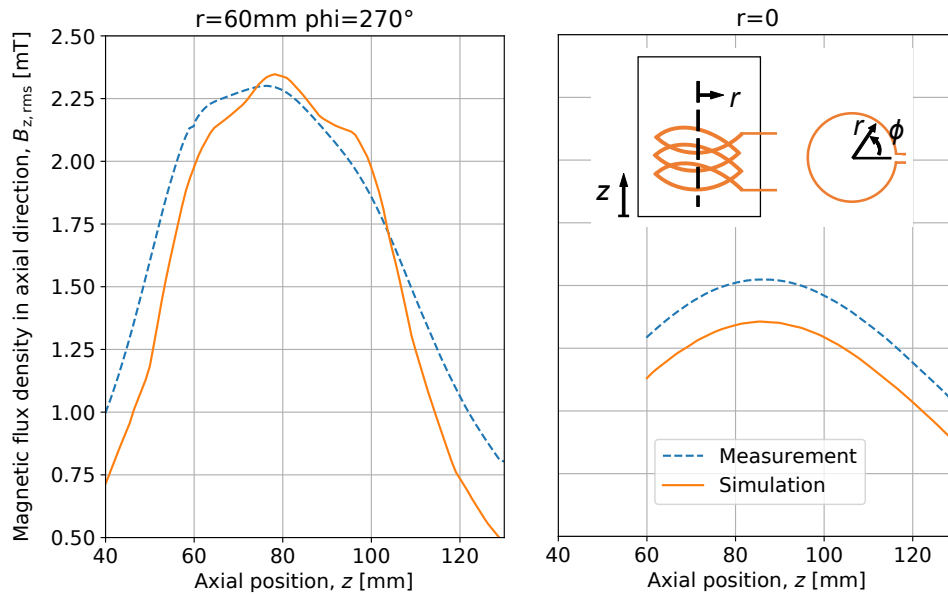


Figure 10: Comparison of simulation and measurement results for magnetic field intensity (empty coil).

4. Case study: energy flow in an industrial Czochralski furnace

The validated numerical model was used to simulate the growth of a 6 inch Si crystal in a 13.5 inch fused silica crucible using an industrial-scale furnace with a KRISTMAG heater-magnet module [30]. The computational domain is shown in Figure 11. See [28, 31] for further details of the model. The heater-magnet module consists of three side heaters and an additional bottom heater, as indicated in the figure. All heaters are made of graphite and are attached to water-cooled current supplies. In a reference experiment at the IKZ, a crystal was grown from 14.8 kg molten silicon under 20 mbar argon atmosphere. The end of the starting cone was chosen as growth stage for the steady-state simulation. The main objective of the simulations was to visualize the flow of heat inside the furnace and to identify energy saving potentials. Given the low gas pressure and limited influence of the melt flow on the global heat transfer [28], the effect of heat convection in gas and melt was neglected.

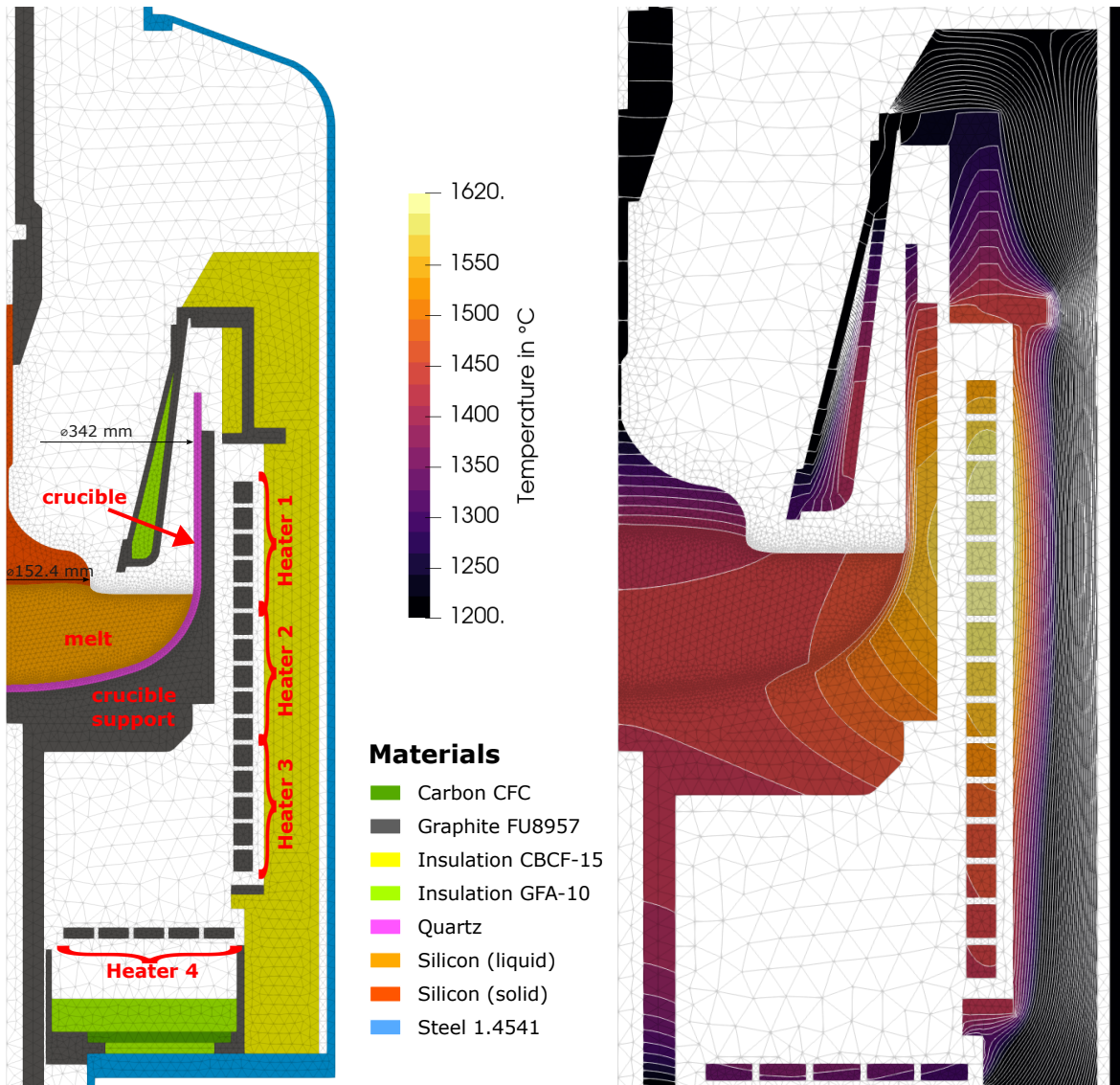


Figure 11: LEFT: Computational domain of industrial-scale silicon growth process; RIGHT: Computed temperature field. The temperature difference between the isotherms is 20 K. Note that values below 1200 °C are truncated in the color scale and appear as black.

The simulation results indicate $P = 26.0$ kW total heating power, approximately 8% lower

than measured in the experiment, possibly due to losses in cables and connections. Further experimental data on heating and cooling rates for this furnace were not available. Based on the simulation results, the growth process has an energy intensity of $e = 10.4$ kWh/kg, within the range shown in Figure 1. In Figure 12, the flow of heat in the furnace is visualized based on the simulation results. It can be seen that less than 1/3 of the total heating power (8.2 kW) is delivered to the crucible support, of which roughly 70% is transferred to the crucible. In other words, little more than 20% of the total heating power is delivered to the crucible. Almost 68% of the total power (17.8 kW) is transferred to the insulation. Almost 70% of the power delivered to the crucible (4.1 kW) is then radiated off the crucible, leaving only 1.7 kW flowing into the melt (approximately 6% of the total heating power).

The thermal inefficiency of the heating process can be clearly seen from Figure 12 along with the temperature field shown in Figure 11. Although there is room for optimizing the heater size and shape as well as the shape and location of insulation and heat shield, resistance heating is inherently inefficient as it entails large, high-temperature surfaces, i.e. the heater, that radiate heat in all directions. Efforts to improve the insulation design could entail not only the thickness, which is limited by the available space, but also the geometry (radiation view factors) and material properties (higher reflectivity). Recently, Qi et al. [32] used numerical simulations to study heat flows in an industrial Czochralski growth furnace for 300 mm silicon crystals with resistance heating. The electrical connections (“electrodes”) of the resistance heater have been identified as a possibility to reduce power loss in the furnace [32]. It should be noted that induction heating would also require optimization if applied to such a silicon growth process. For example, Lorentz forces induced in the melt may be significantly higher than with resistance heaters and influence both heat convection and impurity transport in the melt.

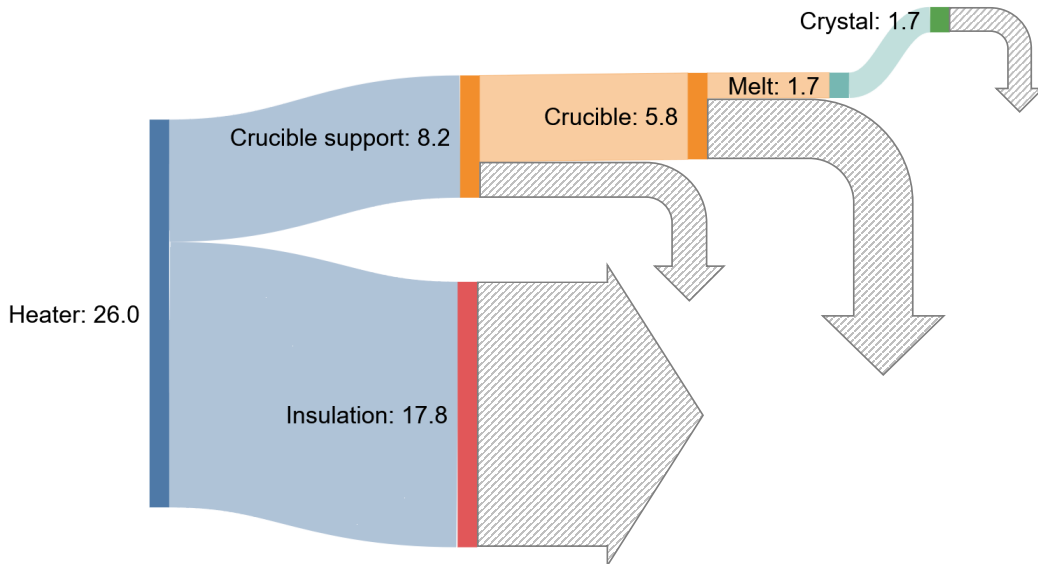


Figure 12: Energy flow [kW] in the furnace (crystallization rate: 2.5 kg/h). Hashed arrows represent radiation to the furnace walls. Plot created using SankeyMATIC [33].

5. Conclusion

Semiconductor crystal growth is an energy-intensive process. Theoretical estimates and representative data from the industry suggest that the energy intensity of silicon crystal growth is as much as 20 times the thermodynamically required limit. The first step towards energy-efficient crystal growth is mapping the flow of energy in the crystal growth furnace and identifying the pathways of energy loss. The present work studied the energy performance of crystal growth from melt using the Czochralski method. Measurements of heating and cooling power were performed in a small-scale research furnace with resistance and induction heating. The measurement results confirm that induction heating has a much higher energy efficiency, suggesting as much as 35% decrease in the energy intensity by switching to induction heating. Using a validated model, numerical simulations were made of an industrial-scale furnace. The simulation results demonstrate great potential for improving the thermal design of the hot zone, where little more than 20% of the total heating power is delivered to the crucible.

It is expected that the importance of energy efficiency in semiconductor production will continue to rise, driven by a combination of environmental and financial concerns. Given the high share of crystal growth in the overall energy demand of the production chain and the demonstrated room for improvement, there is a lot to be gained by revisiting the thermal design of the furnace. Efforts to improve the insulation design can entail increasing the insulation thickness as well as optimizing geometry and using materials with higher reflectivity. Moreover, while induction heating has so far been mostly limited to oxides and fluorides, increased energy efficiency can motivate wider adoption of induction heating for silicon.

Acknowledgments

Vincent Funke and Josef Pal supported the measurements while Dirk Suchland and Adrian Wagner (all IKZ) provided valuable help with the furnace and generator hardware. We also thank Frank Mosel (PVA TePla) and Iason Tsiapkinis (IKZ) for insightful discussions about the CZ process. This study received funding from the European Research Council (ERC) under the European Union’s Horizon 2020 research and innovation programme (grant agreement No 851768).

Appendices

Appendix A. Energy intensity of silicon crystal growth

Energy intensity of industrial processes

With the effective heating power of the furnace, P , known, the energy intensity of growth, e is calculated as:

$$e = \frac{P}{\rho u (\pi D^2 / 4)}$$

where $\rho = 2330 \text{ kg/m}^3$ is the density of silicon, and u and D are the pull rate and crystal diameter, respectively. The denominator of the right-hand side is thus the rate of crystallization in kg/s. The representative values listed in Table A.2, chosen based on the specifications (power rating) of some commercial furnaces, e.g. [34, 35], were used to obtain estimates of e for the Czochralski (CZ) and Floating Zone (FZ) processes.

Table A.2: Representative growth parameters for the Czochralski (CZ) and Floating Zone (FZ) processes.

Process	P [kW]	D [mm]	u [mm/min]
CZ	100, 200, 500	200, 300, 450	1, 2
FZ	100, 120	100, 200	5

Thermodynamic limit

A thermodynamic (idealized) limit for the energy required for the Czochralski growth of silicon crystals can be estimated as the sum of the energy required for three purposes: i) heating silicon to its melting point, ii) melting silicon, and iii) maintaining temperature gradients in the melt needed for a stable growth process. In the equation below, these three components are represented, respectively, by e_{sens} , the specific sensible heat required to bring silicon to its melting point, e_{lat} , the specific enthalpy of fusion of silicon, and e_{cond} , the diffusive heat flux corresponding to typical gradients in the melt normalized by the rate of crystallization [kg/(m²s)]:

$$\begin{aligned} e_0 &= e_{\text{sens}} + e_{\text{lat}} + e_{\text{cond}} \\ &= C_p (T_m - T_0) + e_{\text{lat}} + \frac{k (-\Delta T / \Delta z)_{\text{melt}}}{\rho u} \end{aligned}$$

With $C_p = 1037 \text{ kJ/(kg K)}$, $T_0 = 20 \text{ }^\circ\text{C}$, $T_m = 1410 \text{ }^\circ\text{C}$, $e_{\text{lat}} = 1800 \text{ kJ/kg}$, $k = 62 \text{ (W/m K)}$, $\rho = 2330 \text{ kg/m}^3$, $u = 1 \text{ mm/min}$, and $(\Delta T / \Delta z)_{\text{melt}} \sim -5 \text{ K/cm}$ [36];

$$\begin{aligned} e_{\text{sens}} &\approx 0.4 \text{ kWh/kg} \\ e_{\text{lat}} &\approx 0.5 \text{ kWh/kg} \\ e_{\text{cond}} &\approx 0.2 \text{ kWh/kg} \\ \Rightarrow e_0 &\approx 1.1 \text{ kWh/kg} \end{aligned}$$

During crystallization, only e_{cond} is strictly needed.

Appendix B. Calibration and accuracy of Hall sensor

Calibration

A Helmholtz coil comprised of two copper coils with one winding each ($N = 1$) and a radius of $r = 52.5$ mm was used to calibrate the Hall sensor. The Helmholtz coil was connected to the oscillator, outside the furnace. A pre-coil was added in series to adjust the frequency. See Fig. B.13. Measurements were performed at two frequencies, $f = 16.3$ kHz and $f = 12.4$ kHz, by using two different pre-coils. Comparing the Hall sensor signal with and without a shield between the two coils, it was ensured that the pre-coil does not have a significant effect on the magnetic field inside the Helmholtz coil. The current passing through the coil, I , was measured using a Rogowski coil (Chauvin Arnoux MA200). At either frequency, the current was varied between approximately 30 and 130 A_{rms} to induce a range of magnetic flux densities corresponding to measurements in the furnace.

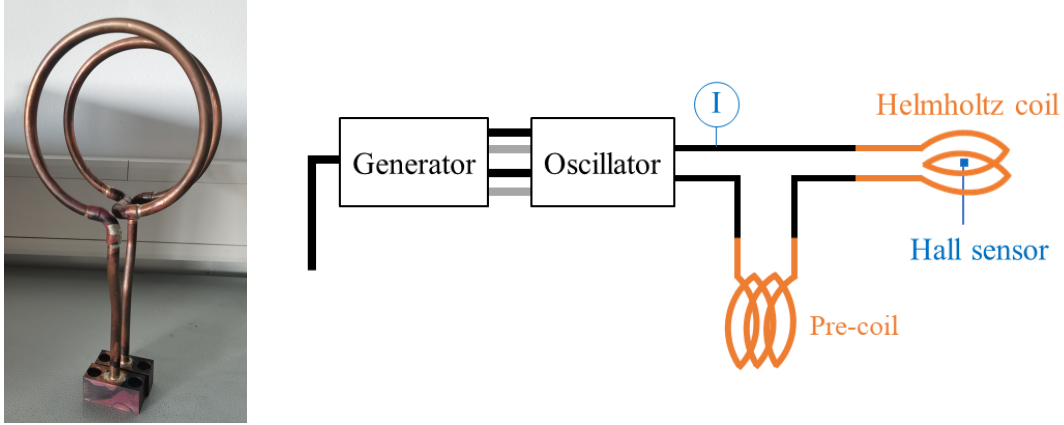


Figure B.13: LEFT: photo of Helmholtz coil, RIGHT: schematic of calibration setup.

With I known, the analytical solution for the magnetic field density of the Helmholtz coil, shown in Equation B.1 [37], was used to estimate the magnetic flux density in the axial direction at the midpoint between the two coils. The measured signal (Hall voltage) from the sensor, U_{Hall} , was then compared to B_{theory} , in order to obtain the calibration factor, k . See Equation B.2.

$$B_{\text{theory}} = \frac{8}{\sqrt{125}} \left(\frac{\mu_0 N I}{r} \right) \quad (\text{B.1})$$

$$k = \frac{B_{\text{theory}}}{U_{\text{Hall}}} \quad \left[\frac{\text{mT}}{\text{mV}} \right] \quad (\text{B.2})$$

The calibration results are shown in Figure B.14. The deviation of the measurement results (up to $\sim 10\%$) from the sensor specification [38] could be attributed to the limited penetration depth of the magnetic field at higher frequencies. An in-depth analysis of such effects was out of the scope of the present study. A similar calibration procedure for induction coil probes has achieved an accuracy of 2% [39]. Based on the present calibration results, $k = 0.0342$ mT/mV was used for the measurements in the furnace ($f \approx 14$ kHz).

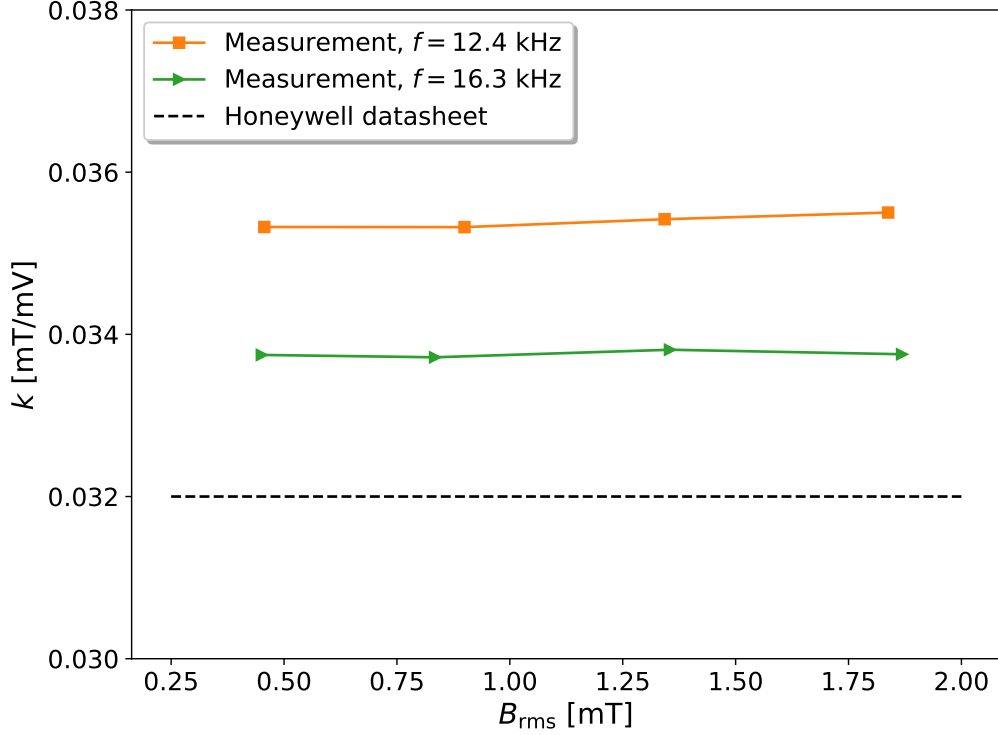


Figure B.14: Calibration factor of Hall sensor.

Accuracy

Given the relatively high accuracy of the current and voltage measurements, the main sources of uncertainty in the magnetic field measurements are geometric, entailing two separate factors. First, the orientation of the Hall sensor in both calibration and measurement. Second, the geometry of the Helmholtz coil, most importantly the coil diameter, spacing and orientation. It is estimated that these two geometric effects could cause up to respectively 2% and 10% uncertainty in the measured magnetic field density.

Finally, it must be noted that the rotation and translation speeds of the shaft are not constant in each scan, especially at the beginning. This was neglected in determining the axial and circumferential positions of the sensor, introducing additional uncertainty to the results shown in Figure 10.

References

- [1] J. Friedrich, W. von Ammon, G. Müller, Czochralski growth of Silicon crystals, in: *Handbook of Crystal Growth*, Elsevier, 2015, pp. 45–104. doi:10.1016/B978-0-444-63303-3.00002-X.
- [2] Z. Galazka, Growth measures to achieve bulk single crystals of transparent semiconducting and conducting oxides, in: *Handbook of Crystal Growth*, Elsevier, 2015, pp. 209–240. doi:10.1016/B978-0-444-63303-3.00006-7.
- [3] E. A. Brandes, G. B. Brook, *Smithells metals reference book*, 7th Edition, Butterworth-Heinemann, 1992. doi:10.1016/B978-0-08-051730-8.50019-4.
- [4] S. C. Hu, Y. K. Chuah, Power consumption of semiconductor fabs in Taiwan, *Energy* 28 (8) (2003) 895–907. doi:10.1016/S0360-5442(03)00008-2.
- [5] O. Burkacky, S. Göke, M. Nikolka, M. Patel, P. Spiller, Sustainability in semiconductor operations: Toward net-zero production, Tech. rep., McKinsey & Co. (2022). URL <https://www.mckinsey.com/industries/semiconductors/our-insights/sustainability-in-semiconductor-operations-toward-net-zero-production>
- [6] C. Robertson, J. Stein, J. Harris, M. Cherniack, Strategies to improve energy efficiency in semiconductor manufacturing, in: *ACEEE Summer Study on Energy Efficiency in Industry*, Saratoga Springs, USA, 1997. URL https://www.aceee.org/files/proceedings/1997/data/papers/SS97_Panel1_Paper27.pdf
- [7] B. Gopalakrishnan, Y. Mardikar, D. Korakakis, Energy analysis in semiconductor manufacturing, *Energy Engineering* 107 (2) (2010) 6–40. doi:10.1080/01998591009709867.
- [8] Electricity 2024 – Analysis and forecasts to 2026, Tech. rep., International Energy Agency (2024). URL <https://www.iea.org/reports/electricity-2024>
- [9] M. Takla, N. Kamfjord, H. Tveit, S. Kjelstrup, Energy and exergy analysis of the silicon production process, *Energy* 58 (2013) 138–146. doi:10.1016/j.energy.2013.04.051.
- [10] S. Riepe, S. Nold, P. Brailovsky, P. Krenckel, L. Friedrich, S. Janz, R. Preu, Cast-mono silicon wafers for a sustainable PV market growth, in: *37th European PV Solar Energy Conference and Exhibition*, 2020. URL <https://www.ise.fraunhofer.de/content/dam/ise/de/documents/publications/conference-paper/37th-eupvsec-2020/Riepe.2AO43.pdf>
- [11] J. O. Odden, G. Halvorsen, H. Rong, Comparison of the energy consumption in different production processes for solar grade silicon, in: *Silicon for the Chemical and Solar Industry IX*, Oslo, Norway, 2008. URL https://www.researchgate.net/publication/267944632_Comparison_of_the_energy_consumption_in_different_production_processes_for_solar_grade_silicon

- [12] Z. Nie, Y. Wang, C. Wang, Q. Guo, Y. Hou, P. A. Ramachandran, G. Xie, Mathematical model and energy efficiency analysis of Siemens reactor with a quartz ceramic lining, *Applied Thermal Engineering* 199 (2021) 117522. doi:10.1016/j.applthermaleng.2021.117522.
- [13] Mineral commodity summaries, Tech. rep., U.S. Geological Survey (2024).
URL <https://www.usgs.gov/centers/national-minerals-information-center/mineral-commodity-summaries>
- [14] A. Hasanbeigi, L. Price, N. Aden, Z. Chunxia, L. Xiuping, S. Fangqin, A comparison of iron and steel production energy intensity in China and the U.S., in: *ACEEE Industrial Summer Study*, New York, USA, 2011.
URL <https://www.osti.gov/servlets/purl/1210892>
- [15] Aluminium - Sustainability information, Tech. rep., Bundesanstalt für Geowissenschaften und Rohstoffe (2020).
URL https://www.bgr.bund.de/EN/Gemeinsames/Produkte/Downloads/Informationen-Nachhaltigkeit/aluminium_en.html
- [16] W. T. Choate, J. A. S. Green, U.S. aluminum production energy requirements: Historical perspective, theoretical limits, and new opportunities, Tech. rep., American Council for an Energy-Efficient Economy (2003).
URL https://www.aceee.org/files/proceedings/2003/data/papers/SS03_Panel1_Paper02.pdf
- [17] A. Enders-Seidlitz, J. Pal, K. Dadzis, Model experiments for Czochralski crystal growth processes using inductive and resistive heating, *IOP Conference Series: Materials Science and Engineering* 1223 (1) (2022) 012003. doi:10.1088/1757-899X/1223/1/012003.
- [18] S. Foroushani, A. Wintzer, K. Dadzis, In-situ Measurement of Emissivity in Crystal Growth Furnaces, in: *International Heat Transfer Conference 17*, 2023. doi:10.1615/IHTC17.380-70.
- [19] Chauvin Arnoux, Current clamps catalogue.
URL <https://www.chauvin-arnoux.com/sites/default/files/documents/chauvin-arnoux-current-clamps-catalogue.pdf>
- [20] Keysight technologies, Data Sheet: N2790A 100 MHz, N2791A 25 MHz and N2891A 70 MHz High-voltage differential probes.
URL <https://www.keysight.com/us/en/assets/7018-02105/data-sheets/5990-3780.pdf>
- [21] Testec, Instruction manual: TT-SI-9101.
- [22] ifm, Data Sheet: SV4200 Vortex flow meter with display.
URL <https://www.ifm.com/de/de/product/SV4200>
- [23] ifm, Data Sheet: SM8020 Magnetic-inductive flow meter.
URL <https://www.ifm.com/de/de/product/SM8020>
- [24] Open source software.
URL <https://github.com/ElmerCSC/elmerfem>

- [25] A. Enders-Seidlitz, J. Pal, K. Dadzis, Development and validation of a thermal simulation for the Czochralski crystal growth process using model experiments, *Journal of Crystal Growth* 593 (2022) 126750. doi:10.1016/j.jcrysgro.2022.126750.
- [26] P. Råback, M. Malinen, J. Ruokolainen, A. Pursula, T. Zwinger, *Elmer Models Manual* (2023).
URL <https://www.elmerfem.org/blog/documentation/>
- [27] C. Geuzaine, J.-F. Remacle, Gmsh: A 3-D finite element mesh generator with built-in pre- and post-processing facilities, *International Journal for Numerical Methods in Engineering* 79 (11) (2009) 1309–1331. doi:10.1002/nme.2579.
- [28] A. Wintzer, Validation of multiphysical models for Czochralski crystal growth, Ph.D. thesis, TU Berlin, Berlin (2024).
URL <https://doi.org/10.14279/depositononce-20957>
- [29] Open source software.
URL https://github.com/nemocrys/opencgs_examples
- [30] C. Frank-Rotsch, N. Dropka, F.-M. Kießling, P. Rudolph, Semiconductor crystal growth under the influence of magnetic fields, *Crystal Research and Technology* 55 (2) (2020) 1900115. doi:10.1002/crat.201900115.
- [31] Open source software.
URL https://github.com/nemocrys/opencgs_examples/tree/main/kristmag-si_2D-3D
- [32] C. Qi, J. Wang, D. Li, Z. Li, J. Li, J. Wang, Y. Wen, L. Wang, Z. Jiang, L. Liu, Study on power consumption and heat transfer paths in czochralski silicon crystal growth based on global 3d numerical simulation, *CrystEngComm* 26 (2024) 5531–5540. doi:10.1039/D4CE00690A.
- [33] Open source software.
URL <https://sankeymatic.com/>
- [34] PVA TePla, Czochralski crystal-growing systems SC28 and CGS1218.
URL <https://www.pvatepla-cgs.com/en/machines/crystal-systems-czochralski/>
- [35] PVA TePla, Float-Zone crystal-growing systems FZ-30 and FZ-35.
URL <https://www.pvatepla-cgs.com/en/machines/float-zone-systems/>
- [36] X. Huang, T. Taishi, T. Wang, K. Hoshikawa, Measurement of temperature gradient in czochralski silicon crystal growth, *Journal of Crystal Growth* 229 (2001) 6–10. doi:10.1016/S0022-0248(01)01040-5.
- [37] S. Tumanski, Magnetic sensors, in: *Handbook of Magnetic Measurements*, CRC Press, 2016, p. 159–256.
- [38] Honeywell, Data Sheet: SS490 Series Linear Hall-effect Sensor ICs.
URL <https://automation.honeywell.com/gb/en/products/sensing-solutions/sensors/magnetic-sensors/ss490-series-linear-sensor-ics>

- [39] I. Tsiapkinis, A. Wintzer, K. Dadzis, Validation of 3D and 2D thermal and electromagnetic models for high-frequency induction heating in crystal growth processes, *Journal of Crystal Growth* 643 (2024) 127800. doi:10.1016/j.jcrysgro.2024.127800.